CHAPTER-5

The 4f-2p-3d Orbital Overlap Formed in a CeO_2/CeCo-LDH Heterostructure Derived from a Metal-Organic Framework for Improved Water Oxidation

This study demonstrates a simple technique for synthesizing a self-supported heterostructure catalyst system, CeO_2/Ce-Co-LDH (CeCo-x, where x = 1, 2, 3), using nickel foam-supported ZIF-67. During hydrothermal treatment, the incorporation of Ce into Co-LDH led to a 4f-2p-3d orbital overlap and the formation of a heterojunction between CeO_2 and CeCo-LDH. Among all synthesized CeCo-x catalysts, CeCo-2 exhibited outstanding OER activity, producing a current density of 50 mA cm^{-2} at a very low overpotential of 220 mV. The 4f-2p-3d orbital overlap modulated the electronic structure, while the heterostructure facilitated efficient charge transport during the OER process. This overlap demonstrated more effective delocalization of π-electron density over the metal center via oxide bridging compared to the 3d-2p-3d overlap. Consequently, the CeO_2/Ce-Co-LDH heterostructures showed excellent OER performance and stability.

5.1. Introduction

Strategies such as electronic structure modulation, creation of cationic and anionic vacancies, and formation of heterostructures have been reported to enhance water oxidation activity.[1] [2] [3] Since the M-O moiety in LDH serves as a catalytically active site for the nucleophilic attack of OH^-, leading to the formation of an O-O bond therefore modulating the local atomic and electronic structure of the M-O bond could effectively enhance the OER activity.[2] Enhancing the electrochemical performance of LDHs can be effectively achieved by modulating the 3d (TM)-2p (O) orbital overlap through the introduction of a heteroatom.[4] Extensive investigation was conducted by several research group to explore the impact of introducing high-valent d-block metal ions (Cr^{VI}, V^{V}, Fe^{III}, Mo^{VI}) on the electronic structure of LDHs for improved OER performance.[5] [6] However, incorporating a 4f/5f-block metal ion into 3d-transition metal-based layered double hydroxides (LDHs) could be the most effective method to achieve nf-2p-3d orbital hybridization, instead of the typical nd-2p-3d hybridization, thereby modifying the electronic structure of LDHs.[7][8][9] The substantial energy disparity between the 3d and 4f/5f orbitals can enhance the charge transfer process through electronic structure modulation. Recently, 5f (U) and 4f (Ce) metal ions have been introduced through doping or substitution in 3d TM oxides or hydroxides to enhance OER activity.[7][9][8] Additionally, it has been observed by several research group that the charge transfer qualities through the interface are improved by the development of a heterostructure with LDHs.[10]

Inspired by the aforementioned studies, we have developed a simple procedure to synthesize a CeO_2/CeCo-LDH heterostructure through a single-step conversion of zeolitic imidazolate framework-67 (ZIF-67, a metal-organic framework MOF). The Lewis acid Ce^{III} initiates the hydroxylation of ZIF-67 into CeCo-LDH whereas the hydrolysis of Ce^{III} forms CeO_2, resulting in

the formation of CeO_2/CeCo-LDH heterostructure **(Scheme 5.1)**. The oxygen-deficient characteristic of CeO_2 enhances the adsorption and dissociation of water on the catalyst surface, whereas the interface formed between CeCo-LDH and CeO_2 regulates the process of charge transfer. The introduction of $Ce^{III/IV}$ into Co-LDH modifies the electrical structure by diminishing the electron density of $Co^{II/III}$ ions. More accurately, intervalence charge transfer between the Ce (4f) and Co (3d) atoms regulates the electronic structure in CeCo-LDH.[10] The 4f-2p-3d orbital hybridization is employed to enhance the OER activity by modulating the electron density on the 3d orbital of the Co-ion.

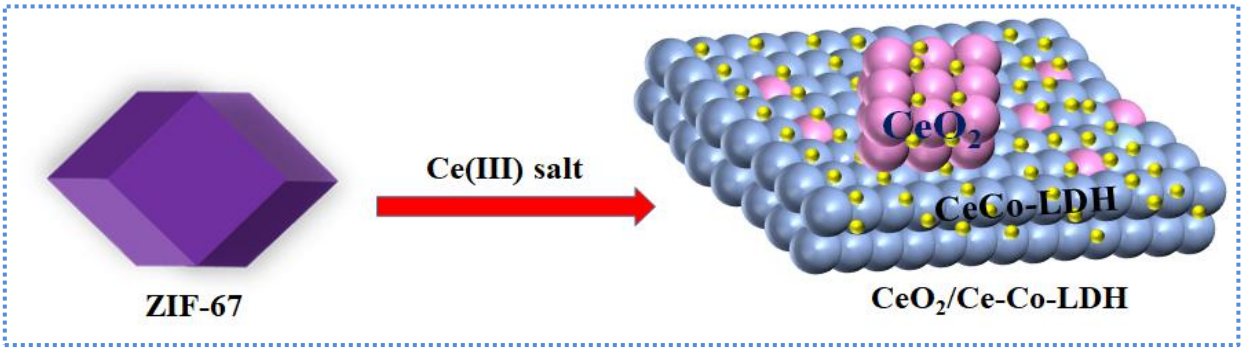

Scheme 5.1. Schematic diagram showing the transformation of ZIF-67 into CeCo-x (x = 1, 2, 3) by a Lewis acid Ce^{III}-assisted hydroxylation method.

In this study, we have employed a single-step method to integrate the aforementioned approaches, incorporating Ce into the structure of Co-LDH and forming a heterostructure between CeO_2 and CeCo-LDH. Moreover, employing ZIF-67 as the precursor provided benefits such as a high electrochemical surface area (ECSA) and accessible active sites, hence enhancing mass transfer.[11] Recently, our group and others have also demonstrated the superior performance of MOF-derived LDHs towards electrochemical water splitting.[12][13]

The integration of aforementioned factors led to a significant enhancement in the OER activity of CeO_2/CeCo-LDH (CeCo-x, x = 1, 2, 3) catalysts compared to Co-LDH, CeO_2 + Co-

LDH, and CeCo-LDH catalysts. CeCo-2 exhibited superior OER catalytic activity as it produces 500 mA cm^{-2} OER current density at 320 mV overpotential, which is noticeably lower than most of the LDHs reported in the literature.[14] Additionally, CeCo-2 demonstrated durability over 100 hours under chronoamperometric (CA) conditions, continuously producing oxygen.

5.2. Chemicals

Cobalt chloride hexahydrate was purchased from Sigma Aldrich (99.9%). Urea (99.5%) and ammonium fluoride (98%) were bought from SRL as in previous chapter-3. Cerium nitrate nonahydrate was purchased from SRL. All chemicals were used without any further purification. Nickel foam was purchased from AXYS technology. Double distilled water was used for all the experiments and electrochemical measurements.

5.3. Instruments

The crystallinity and phase identification of the synthesized catalysts were confirmed by room temperature X-ray diffraction (Rigaku Miniflex 600) using Cu-K alpha radiation (1.54 Å). The IR spectra were recorded at Nicolet iS5 FTIR spectrometer in attenuated total reflection (ATR) mode in the range between 400- 4000 cm^{-1}. The XPS spectra have been measured using a Thermo Fisher Scientific instrument with Al K-alpha radiation operated at 150 W. Microstructure and compositional analyses of the prepared materials were examined with the help of Field emission scanning electron microscopy (Nova Nano SEM 450) equipped with an EDS System and the interlayer d-spacing of the synthesized catalysts was obtained by taking HR-TEM images (FEI TECNAI G2 20 TWIN) operated at 300 kV.

5.4. Experimental

5.4.1. Activation of nickel foam

Nickel foam was activated by the methods mentioned in previous chapter.

5.4.2. Synthesis of cobalt hydroxide carbonate template on nickel foam (Co-HC@NF)

Co-HC@NF was synthesized by the method mentioned in previous chapter.

5.4.3. Synthesis of ZIF-67@NF

Mentioned in previous chapter.

5.4.4. Synthesis of CeCo-2

A clear solution of $Ce(NO_3)_3 \cdot 6H_2O$ (0.2 mmol) was prepared by dissolving it in a mixed solution of iso-propanol and ethylene glycol (8:2) with a total volume of 12 mL. This clear solution was then transferred into a Teflon-lined autoclave. Subsequently, ZIF-67@NF was immersed vertically into the reaction mixture, and the autoclave was sealed. The sealed autoclave was placed in an electric oven and maintained at 120°C for 5 hours. After completion of the reaction time, the autoclave was allowed to cool naturally to room temperature. Finally, the CeCo-2 deposited nickel foam was dried overnight at 60°C.

Similarly, CeCo-1 and CeCo-3 were obtained by changing the amount of $Ce(NO_3)_3.6H_2O$ **(see Table 4.1)**.

5.4.5. Synthesis of CeO_2+Co-LDH@NF

The CeO_2+Co-LDH@NF catalyst was synthesized using Co-LDH as a precursor. Initially, 0.2 mmol of $Ce(NO_3)_3 \cdot 6H_2O$ was dissolved in a mixed solution of iso-propanol and ethylene glycol (8:2) with a total volume of 12 mL. The resulting solution was then transferred into a 50 mL Teflon-lined autoclave. A film of Co-LDH was vertically immersed in the solution, and the autoclave was sealed. The sealed autoclave was placed in an electric oven and maintained at 120°C for 5 hours. After completion of the reaction, the autoclave was allowed to cool to room temperature. The CeO_2+Co-LDH@NF catalyst was subsequently dried overnight at 60°C.

5.4.6. Synthesis of CeCo-LDH

The CeCo-LDH catalyst was synthesized by immersing ZIF-67@NF in a 15 mL vial containing a 5 mL solution of Ce(III) salt in a combination of isopropanol and ethylene glycol (8:2). The reaction mixture was kept at room temperature for a period of 10 hours. After the reaction time period ended, the catalyst that was produced was washed with isopropanol and then dried at a temperature of 60 ^{o}C overnight.

5.4.7. Synthesis of Co-LDH

For this, the synthetic procedure used in chapter 3 was also used in this chapter**.**

Table 5.1. Details of the synthesis of CeCo-x catalysts.

Catalyst	Precursor	Synthesis conditions
Co-LDH	ZIF-67@NF	$CoCl_2.6H_2O$ (0.2 mmol)
CeCo-1	ZIF-67@NF	$Ce(NO_3)_3.6H_2O$ (0.1 mmol)
CeCo-2	ZIF-67@NF	$Ce(NO_3)_3.6H_2O$ (0.2 mmol)
CeCo-3	ZIF-67@NF	$Ce(NO_3)_3.6H_2O$ (0.3 mmol)
CeCo-LDH	ZIF-67@NF	$Ce(NO_3)_3.6H_2O$ (0.2 mmol), at room temperature
CeO_2+Co-LDH	Co-LDH@NF	$Ce(NO_3)_3.6H_2O$ (0.2 mmol)

5.5. Results and discussion

5.5.1. Characterizations of the catalysts

To prepare the self-supported catalyst system, we initially deposited Co hydroxide carbonate (Co-HC) on NF, followed by treatment with 2-methyl imidazole to form ZIF-67@NF. Subsequently, ZIF-67@NF was reacted with different quantities of Ce^{III} salt to synthesize CeCo-x catalysts **(Scheme 5.1 and Table 5.1)**. During the reaction, the Ce^{III} compound functioned as a Lewis acid, enabling the hydroxylation process of ZIF-67. As a consequence, the ZIF-67 structure was

destroyed and CeCo-LDH was formed.

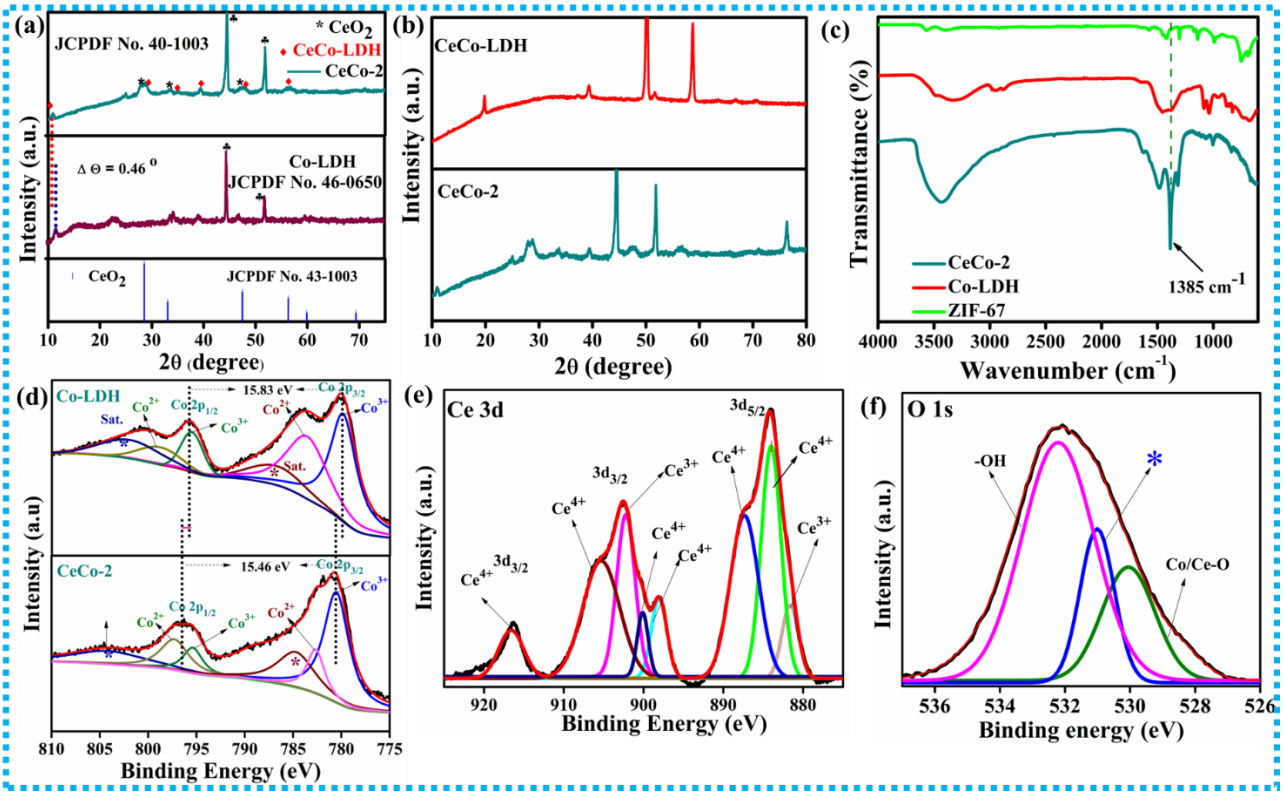

Figure 5.1. (a) Top) The powder X-ray diffraction pattern of CeCo-2 shows two distinct sets of peaks, confirming the presence of two phases. Peaks labelled with * correspond to CeO_2, while peaks marked with ♦ indicate CeCo- LDH. Additionally, ♣ marks denote the presence of nickel foam; (b) The powder X-ray diffraction pattern of CeCo-2 and CeCo-LDH; (c) Fourier transformed infrared (FTIR) spectra of ZIF-67, Co-LDH and CeCo-2. Peak obtained at 1385 cm^{-1} confirms the presence of intercalated carbonate anion between the layers of Ce-Co-LDH; (d) Co 2p XPS of Co-LDH is compared with that of CeCo-2; (e) Ce 3d XPS showing the presence of both Ce^{III} and Ce^{IV} species; (f) O 1s XPS spectrum was deconvoluted into three peaks corresponding to Co/Ce–O, hydroxyl species and oxygen defect sites (*).

At the same time, Ce^{III} underwent hydrolysis to form CeO_2 in the presence of dissolved O_2, resulting in the formation of a CeCo-2 heterostructure. Detailed information about the other catalysts (Co-LDH, CeCo-LDH, and CeCo-LDH + CeO_2) can be found in the provided table **(Table 5.1)**.

Extensive characterization was conducted on the CeCo-2 catalyst, which demonstrated the highest OER activity. The PXRD (powder X-ray diffraction pattern) of the as synthesized catalyst showed two distinct diffraction patterns corresponding to CeCo-LDH and CeO_2 phase **(Figure 5.1a)**. [15] The peaks obtained at 28.5°, 33.5°, 47.24°, and 56.5°, belong to (111), (200), (220), (311), and (222), planes of CeO_2 structure (JCPDS 34-0394) and the peaks at 10.92°, 34.9°, 39.29°, and 47.8°, were ascribed to (003), (012), (015), and (018), planes of the CeCo-LDH (JCPDS 40-0215). A negative shift of 0.46° in 2θ value was detected for the CeCo- LDH component of CeCo-2 compared to Co-LDH **(Figure 5.1b)** .[16] Also, this suggests an increase in the inter-layer distance due to the incorporation of Ce^{III} into Co-LDH. Fourier-transform infrared (FTIR) spectroscopy identified the presence of CO_3^{2-} anions (peak at 1385 cm^{-1}) intercalated between the layers of metal hydroxide to neutralize its positive charge **(Figure 5.1c)**.[16]

Moreover, X-ray photoelectron spectroscopy (XPS) was performed on CeCo-2 to investigate the electronic environments of the elements **(Figure 5.1d)**. The Co 2p XPS spectrum was resolved into two peaks, corresponding to Co $2p_{3/2}$ (780.66 eV) and Co $2p_{1/2}$ (796.25 eV) **(Figure 5.1d)**.[17] Each of these two peaks were subsequently deconvoluted to into Co^{II} and Co^{III} states. The introduction of Ce into Co-LDH led to a notable alteration of the electronic structure, evident in the shift of the $Co2p_{3/2}$ peak towards higher binding energies. The spin-orbit spacing value is also decreased after the Ce incorporation in Co-LDH. The ratio of Co^{III}/Co^{II} in CeCo-2 was calculated to be 1.86 through peak area integration. This value demonstrates that the incorporation of Ce^{III} and Ce^{IV} significantly increases the proportion of Co^{III} relative to Co^{II} in CeCo-2 compared to Co-LDH (where the ratio of Co^{III}/Co^{II} = 1.16). The satellite peaks for Co^{II} have also been detected in the Co 2p XPS of CeCo-2.

Furthermore, a positive shift of 0.98 eV was observed for the Co $2p_{3/2}$ peak relative to Co-

LDH.[16][18] The Co $2p_{3/2}$-Co $2p_{1/2}$ spin-orbit spacing was calculated to be 15.46 eV, indicating the presence of both Co^{III} and Co^{II}. The reduced spin-orbit spacing between Co $2p_{3/2}$ and Co $2p_{1/2}$ suggests a greater presence of Co^{III} in CeCo-2 compared to Co-LDH.

The Ce 3d XP spectra was deconvoluted into the peaks corresponding to Ce $3d_{5/2}$ and Ce $3d_{3/2}$.[19] The peaks were assigned to both Ce^{III} and Ce^{IV} species **(Figure 5.1e)**. The Ce^{IV} to Ce^{III} ratio was determined to be 3.15, indicating a greater concentration of Ce^{IV} compared to Ce^{III} which is of significant importance for the coupling of the 4f-2p-3d orbitals. Furthermore, the observed downward shift of the Ce 3d spectrum in CeCo-2, as compared to CeO_2, suggests a decrease in the positive charge density on the Ce atom which was due to the transfer of electron density from Co^{II} to Ce^{IV}.[20] The O1s XPS spectrum was deconvoluted into three distinct peaks corresponding to the Ce/Co–O bond, -OH species, and oxygen vacancies **(Figure 5.1f)**.[17] The addition of Ce^{III} to CeO_2 caused a substantial increase in the number of oxygen vacancies, resulting in the formation of defect-rich areas in CeO_2, which was also confirmed by TEM analysis **(Figure 5.2m)**. The XPS analyses indicate a significant electronic interaction. The introduction of Ce^{III} into CeO_2 led to a significant augmentation in the quantity of oxygen vacancies, leading to the formation of regions with a high concentration of defects in CeO_2, as demonstrated by TEM examinations

The nanosheet-like shape of CeCo-2 was clearly observed by scanning electron microscopy (SEM) **(Figure 5.2a)**. The energy dispersive X-ray (EDX) mapping revealed the uniform distribution of Co, Ce, O, and C throughout the nanosheets of CeCo-2 **(Figure 5.2h-k).** The TEM images of CeCo-2 revealed transparent ultrathin nanosheets of CeCo-LDH with randomly distributed CeO_2 nanoparticles on them **(Figure 5.2 c-d)**. High-resolution TEM (HR-TEM) revealed the formation of heterojunction between CeO_2 and CeCo-LDH **(Figure 5.2 d)**. The d-spacing of 0.251 nm corresponds to the (012) plane of Ce-Co-LDH, while the d-spacings of 0.321 nm and 0.275 nm

are associated with the (111) and (200) planes of CeO_2, respectively **(Figure 5.2d-g)**.

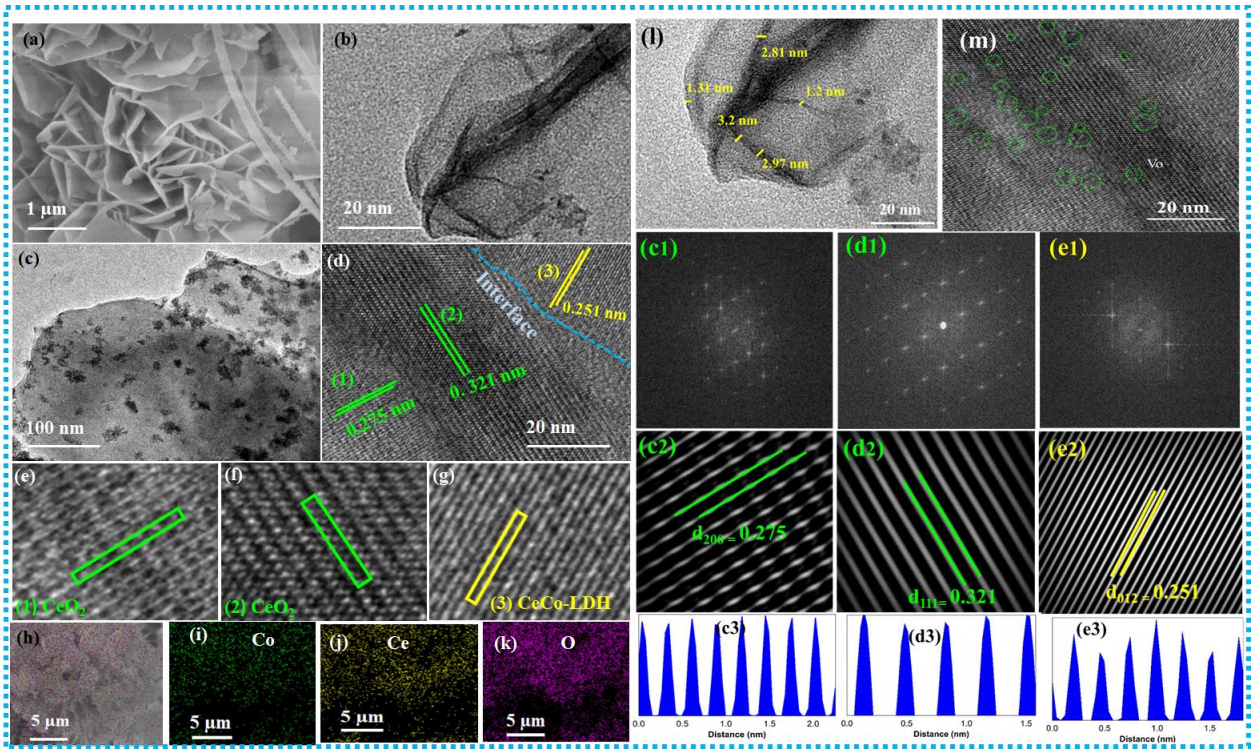

Figure 5.2. (a) SEM image of CeCo-2 on nickel foam; (b) TEM image showing the ultrathin nanosheets of CeCo-2 having an atomic level thickness; (c) TEM image showing the distribution of CeO_2 on CeCo-LDH; (d) HR-TEM image showing the interface formation between CeO2 and Co-LDH; (e)-(g) The lattice spacing corresponding to the region (1), (2) and (3) in the figure (d); (h)-(k) Elemental mapping of CeCo-2 showing the distribution of elements Ce, Co, C, and O; (l) The thickness of vertically grown CeCo-2 nanosheets; (m)) HRTEM image showing the defect rich sites (green circle) in CeO_2 of CeCo-2; (c1)-(e1) FFT of the areas (1), (2), and (3) in the figure (d), respectively; (c2)-(e2) The corresponding inverse FFT images of (c1)-(e1), respectively; (c3)-(e3)The contrast intensity profiles corresponding to the figures (c2)-(e2) showing the lattice parameters.

The thickness of nanosheet was measured to be between 2 and 4 nm **(Figure. 5.2l)**. The atomic-level thickness of these nanosheets provides access to numerous active sites and coordinative and electronic unsaturation, enhancing the binding of intermediates on the catalyst surface and thereby improving catalytic activity. The fast Fourier transformed (FFT) images corresponding to **(Figure**

5.2e-g) and their inverse FFT clearly showed the d-spacings corresponding to CeO_2 and Ce–Co-LDH to form a heterojunction in CeCo-2 **(Figure 5.2c3-e3).**

5.5.2. Electrochemical Activity

To understand the redox behaviour of CeCo-2 and Co-LDH, cyclic voltammetry (CV) was performed **(Figure 5.3a)**. Two peaks related to the oxidation of Co^{II} to Co^{III} (1.10 V vs. RHE) and Co^{III} to Co^{IV} (1.34 V vs. RHE) were identified for CeCo-2 whereas a single peak at a higher potential (1.38 V vs. RHE) was detected for Co-LDH.

In CeCo-2, Ce ions induce modulation of the electronic structure by facilitating electron transfer from Co^{II} to Ce^{IV}, thereby promoting the oxidation of Co^{II} to Co^{III} and subsequently to Co^{IV} **(Figure 5.3a)**. The electrocatalytic oxygen evolution reaction (OER) activities of CeCo-2 and other catalysts were evaluated using linear sweep voltammetry (LSV) in a 1.0 M aqueous potassium hydroxide (KOH) solution **(Figure 5.3b)**. Out of all synthesized catalysts, CeCo-2 exhibited the highest OER activity. The establishment of a heterojunction between CeO_2 and CeCo-LDH had a significant influence on the (OER) activities of all forms of CeCo-x **(Figure 5.3b)**. The formation of a heterojunction enhances charge transfer across the interface and modulates the catalyst's electronic structure. In addition, the catalyst surface can enhance the adsorption of chemical intermediates through the development of heterojunctions. Previous studies have reported enhanced oxygen redox activities of Co/CeO_2 and improved OER and HER activities of CuO/CeO_2 catalysts was obtained due to heterojunction formation.[20] As the amount of Ce^{III} in Co-LDH increased, the overpotential for the OER decreased, reaching an optimal value for CeCo-2, and then increased thereafter **(Figure 5.3c).**Remarkably, CeCo-2 produced a current density of 50 mA cm^{-2} at just 220 mV overpotential, significantly lower than the 360 mV which was required by Co-LDH. Furthermore, CeCo-2 produced a high current density of 500 mA cm^{-2} at only 320 mV,

which is highly significant for the development of industry-scale electrolyzer cells.[21] Although the integration of CeO_2 with Co-LDH (CeO_2 + Co-LDH) formed a heterojunction and demonstrated improved OER activity compared to Co-LDH, it did not achieve the high activity of CeCo-2 **(Figure 5.3g and table 5.1)**.

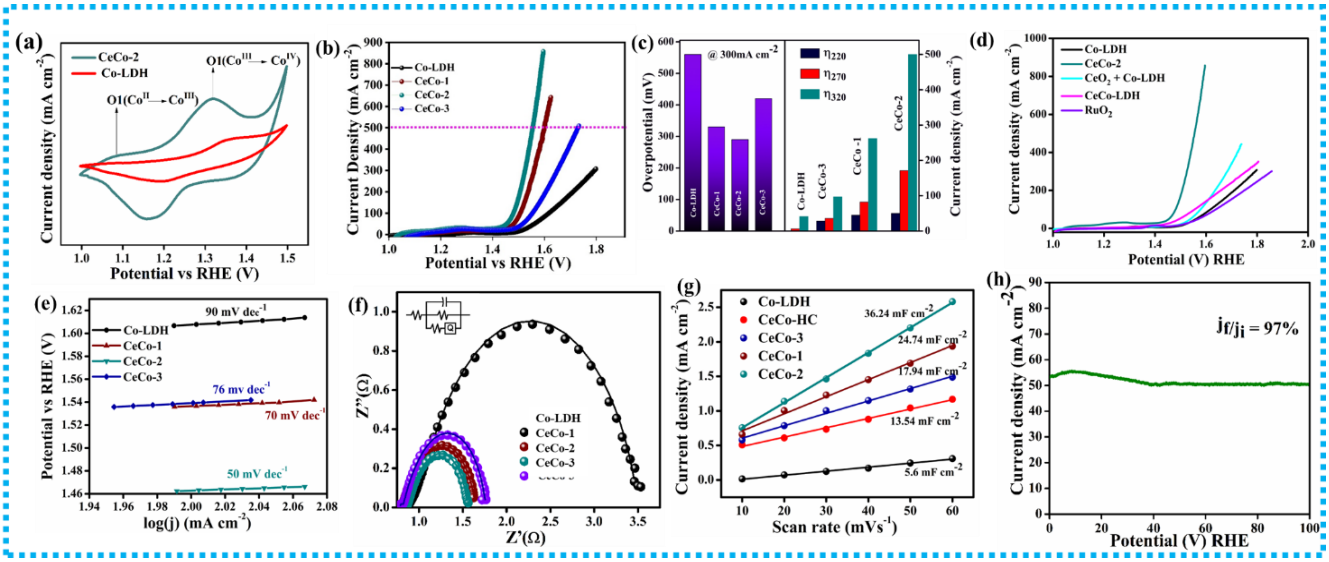

Figure 5.3. (a) CV profiles of CeCo-2 and Co-LDH displaying redox peaks corresponding to the oxidation of Co^{II} to Co^{III} and Co^{III} to Co^{IV} during the OER; (b) Linear sweep voltammetric profiles of the OER for the synthesized catalysts, illustrating enhanced catalytic activity upon Ce introduction into Co-LDH, with CeCo-2 demonstrating the highest activity; (c) Comparative plots of overpotentials and current density for different catalysts, demonstrating CeCo-2's superior performance; (d) LSV profiles for OER of the synthesized catalysts compared to the benchmark catalyst RuO_2, highlighting CeCo-2's superior activity; (e) Tafel plots for the oxygen evolution reaction comparing CeCo-2 with other catalysts. The lowest Tafel slope observed for CeCo-2 indicates the fastest OER kinetics; (f) Nyquist plots for CeCo-2, Co-LDH, CeCo-1, and CeCo-3, revealing the lowest charge transfer resistance for CeCo-2. Spectra were collected at an anodic polarization potential of 1.48 V vs RHE, within a frequency range of 0.01 to 10^6 Hz; (g) Determination of double-layer capacitance (C_{dl}) for Co-LDH, CeCo-1, CeCo-2, and CeCo-3 by plotting (difference in current density)/2 against scan rate; (h) Long-term chronoamperometric OER performance of CeCo-2.

Table 5.2. The OER activities of reported electrocatalysts compared with CeCo-2.

Entry	Catalyst	Current density ($mA\ cm^{-2}$)	Overpotential	Reference
Co-based LDHs				
1	$V_{0.3}$-CoFe-LDH	10	240	[22]
2	CoFeV LDH/NF	10	242	[23]
3	$Co_{0.4}Fe_{0.6}$LDH/g-CN_x	10	270	[24]
4	NiCoV-LDH	10	280	[25]
5	Cr-CoFe-LDHs/NF	10	238	[26]
ZIF-67-derived catalysts				
6	FeCo-LDH@$Co(OH)_2$	10	230	[27]
7	NiFe-LDH/Co-NC-2	10	282	[28]
8	NiFeCo-LDH/CF	10	249	[29]
9	$Fe_{0.4}$Co-LDH@NF	20	190	[16]
Ce-based catalysts				
10	**CeCo-2**	**500**	**320**	**This work**
11	FeOOH/CeO_2 HLNTs	17.6	250	[30]
12	CeO_2/$Co(OH)_2$	10	250	[31]
13	Ni_4Ce_1@CP	10	410	[32]
14	Co_3O_4/CeO_2 NHs	10	270	[33]
15	NiCoCe-LDH/CNT	10	236	[34]
16	Ce-CoFe LDH	10	370	[35]
17	CoO_x(Ce)	10	261	[36]
18	$CoSe_2$/CeO_2	10	288	[37]
19	Se-doped Co_3O_4@CeO_2	50	293	[38]
20	Ce-NiFe-LDH/CNT	10	227	[19]
21	CeO_x/CoS	10	269	[39]
22	Co/Ce Ni_3S_2@NF	10	286	[40]
23	CeO_2-Co_2O_3@NF	50	334	[41]

Therefore, the synthetic method has significant impact on the catalytic activity of the materials. Similarly, the OER performance of CeCo-2 was superior to that of CeCo-LDH and the benchmark catalyst RuO_2 **(Figure 5.3d)**. These results clearly demonstrate that CeCo-2 has distinctive electrochemical characteristics, which are derived from the synthesis of ZIF-67 with the assistance of Ce^{III}. CeCo-2 exhibits a higher overpotential for the oxygen evolution reaction (OER) compared to other cobalt-based layered double hydroxides (LDHs) and catalysts generated from ZIF-67

(Tables 5.2).

Out of all synthesized catalysts, CeCo-2 had the smallest Tafel slope, measuring 50 mV dec^{-1} **(Figure 5.3e)**. This outcome validates that the incorporation of CeO_2 with a high concentration of defects enhances the rate at which charge is transferred during the catalytic process, leading to accelerated kinetics of OER. CeCo-2 exhibited the lowest charge transfer resistance (R_{ct}) as demonstrated by the electrochemical impedance spectroscopy (EIS) **(Figure 5.3f)**.

The electrochemical active surface area was determined by measuring the double-layer capacitance (C_{dl}), and the CeCo-2 sample exhibited the greatest C_{dl} value **(Figure 5.4a)**.

The ECSA normalized OER activity of CeCo-2 demonstrated a remarkable value of 2.53 mA cm^{-2} at 1.59 V vs. RHE **(Figure 5.4b-c)**. This value is comparable to that of highly active OER catalysts reported in the literatures **(Table 5.3).** Also, number of active sites of the as synthesized catalysts were calculated and CeCo-2 exhibited the highest number of active sites **(Figure 5.4e and table 5.4)**. Nevertheless, the turnover frequency (TOF) exhibited a progressive increase with the increase in Ce^{III} ion concentration, reaching its peak value for CeCo-2 (TOF = 9.18 s^{-1}), and thereafter dropped as the concentration of Ce^{III} further increased, following a volcanic trend **(Figure 5.4d-e)**.

To understand the main reason behind these observations, we conducted a comparative evaluation of their Tafel slopes and ECSA**.** The CeCo-x catalysts showed decreased Tafel slope values and increased ECSA as the Ce content was increased from Co-LDH to CeCo-2 **(Figure 5.4a)**.

This trend indicates an increased presence of active sites and enhanced kinetics, promoting the transport of charge and mass carriers. However, the higher Ce loading led to a reduction in available active cobalt sites in the catalyst. At the same time, the high loading of CeO_2 on Ce-Co-LDH introduced a strong barrier to electron transmission, as evidenced in the Tafel slope and EIS

(Figure 5.3 e and f). To assess catalytic stability, the OER activity of CeCo-2 was measured under chronoamperometric (CA) conditions at high current density for 100 hours, revealing a negligible (0.3%) loss in current density compared to the initial value **(Figure 5.3h)**.

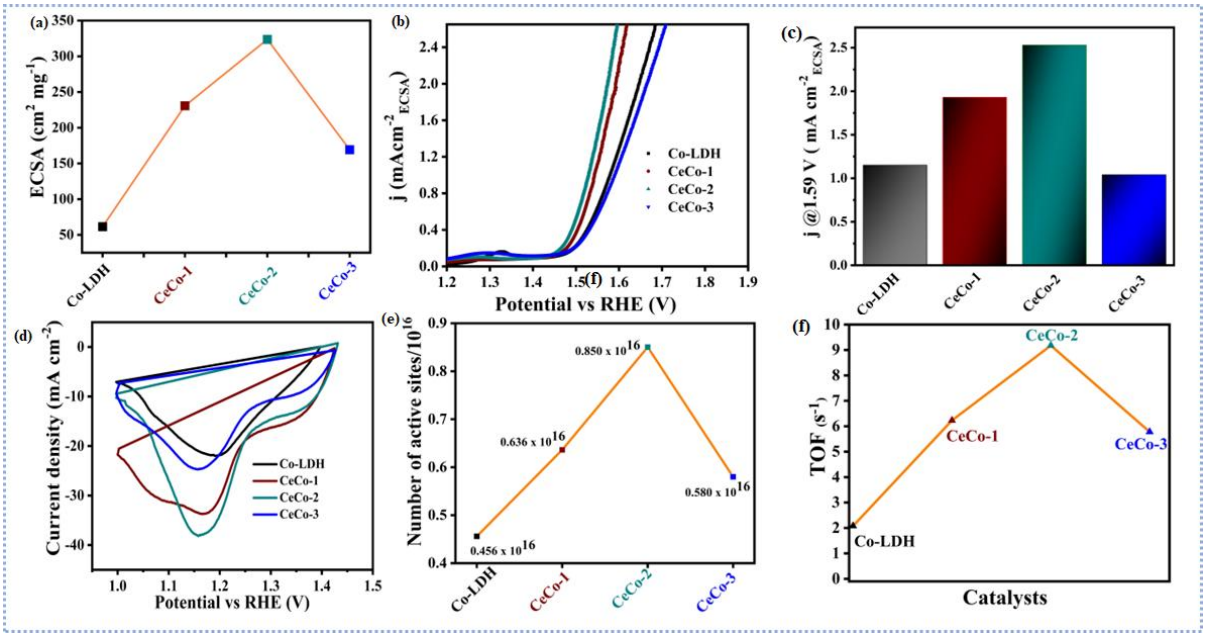

Figure 5.4. (a) The ECSA of the catalysts increased with higher Ce content, reaching a peak for CeCo-2 and decreasing with further increases in Ce(III); (b) Normalized current density based on ECSA for the catalysts; (c) Plot of ECSA-normalized current density at 1.59 V, demonstrating CeCo-2 as the most active catalyst; c) Plot of ECSA-normalized current density at 1.59 V, demonstrating CeCo-2 as the most active catalyst; (d) Potential versus current density plots showing the reduction peak used for area integration; (e) Calculation of the number of active sites for the catalysts; (f) Plot showing the turnover frequency (TOF) of the catalysts.

Table 5.3. The determination of C_{dl} and ECSA for different catalysts.

Sr. No.	Catalyst	C_{dl} (mF cm^{-2})	ECSA (cm^2/mg)
1	Co- LDH	5.63	61.45
2	CeCo-1	24.74	230.7
3	CeCo-2	36.24	323.57
4	CeCo-3	17.94	169.24

Table 5.4. ECSA normalized OER activity of reported catalysts compared with CeCo-2.

Entry	Catalysts	Potential (V) RHE	Current density ($mA\ cm^{-2}$ ECSA)	Ref.
1	NiFe-LDH	1.58	0.1	[42]
2	NiOOH	1.6523	10	[43]
3	Co_9S_8/CoO/NC	1.5	0.009	[44]
4	$Ni_{83}Fe_{17}$-ONCAS	1.568	1.0	[45]
5	Ni–Fe NP	1.43	10	[46]
6	Ni/MoO_2@CN	1.59	0.2	[47]
7	NiFe-LDH	1.502	0.1	[48]
8	$Ni(OH)_2$	1.603	0.1	[48]
9	Ni_9FeOOH	1.45	0.028	[49]
10	$Ir_{0.1}$/Ni_9Fe SAC	1.45	0.053	[49]
11	**CeCo-2**	**1.59**	**2.53**	**Our Work**

After 100 hours of chronoamperometric testing, the catalyst underwent PXRD and SEM characterization **(Figure 5.5)**. The PXRD analysis revealed peaks corresponding to Ce-Co-LDH, CeO_2, and Co(O)OH. However, slight agglomeration of CeCo-2 nanosheets was observed after 100 hours of CA testing **(Figure 5.5)**.

Also The redox behaviour of the Ce^{IV}/Ce^{III} couple plays a crucial role in modulating the Lewis acidity of the catalyst, resulting in increased OER activity.[50] Another crucial factor is the overlap of 4f-2p-3d orbitals, involving the pi-orbitals of Ce (4f), O (2p), and Co (3d).[7] In an octahedral field, low-spin Co^{III} exhibits a fully filled t^6_{2g} configuration, leading to electron-electron repulsion with the p-electrons of O^{2-}. On the other hand, Co^{II} ($t^6_{2g}\ e^1_g$) can interchange partial electron density with Co^{III} by bridging O^{2-}.[51] When Ce^{IV} is introduced in the catalyst structure, it encourages a strong p-p interaction to enhance electron transfer from Co^{III} to O^{2-}, and finally to Ce^{IV} **(Figure**

5.5 e). Consequently, delocalization of the pi-electrons is favoured compared to the 3d-2p-3d orbital overlap in Co-LDH. This process promotes the stability of the Co centre in its high oxidation state (IV), which improves OER activity.

Table 5.5. Number of active sites and TOFs of different catalysts.

Sr. No.	Catalyst	Area under the curve (VA)	No. of active sites	TOF (s^{-1})
1	Co-LDH	3.650×10^{-6}	0.451×10^{16}	2.05
2	CeCo-1	5.09×10^{-6}	0.636×10^{16}	6.237
3	**CeCo-2**	$\mathbf{6.802 \times 10^{-6}}$	$\mathbf{0.850 \times 10^{16}}$	**9.177**
4	CeCo-3	5.849×10^{-6}	0.580×10^{16}	5.785

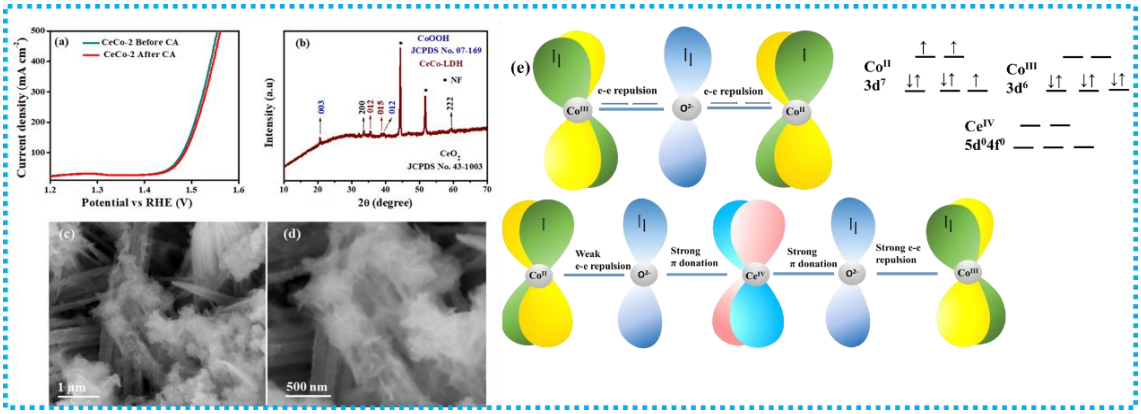

Figure 5.5. (a) LSV curves of CeCo-2 before and after CA, (b) PXRD of CeCo-2 after 100 h CA measurement, and (c-d) SEM images of CeCo-2 after 100 h CA measurement; (e) Schematic representation of π-orbital overlap to promote electron transfer from $Co^{II/III}$ to Ce^{IV} involving O (2p) π-orbital.

5.6. Conclusion

In conclusion, self-supported heterostructure catalysts were effectively synthesized on nickel foam using ZIF-67 as the precursor. Incorporating Ce into Co-LDH modulate the electronic structure of catalyst through 4f-2p-3d orbital overlap, while the heterojunction between CeCo-LDH and CeO_2 regulated the charge transfer mechanism during the OER. The 4f-2p-3d orbital overlap was observed to be more effective in dispersing the p-electron density on the metal centres via oxide

bridges, compared to the 3d-2p-3d orbital overlap. Consequently, the promotion of high-valent Co^{IV}-O species formation facilitated the nucleophilic attack of OH^- and enhanced the OER activity.

5.7. References

[1] L. Tian, Q. Wang, Y. Li, X. Ren, Q. Wei, D. Wu, *Dalt. Trans.* **2022**, *51*, 10552.

[2] B. Singh, A. Indra, *Mater. Today Chem.* **2020**, *16*, 100239.

[3] L. Hong, B. Li, C. Jing, Z. Zhuang, Y. Zhang, H. Huang, Q. Jiang, J. Tang, *J. Environ. Chem. Eng.* **2024**, *12*, 111946.

[4] X. Z. Song, W. Y. Zhu, X. F. Wang, Z. Tan, *ChemElectroChem* **2021**, *8*, 996.

[5] T. Guo, L. Li, Z. Wang, *Adv. Energy Mater.* **2022**, *12*, 1.

[6] Z. Cai, X. Bu, P. Wang, J. C. Ho, J. Yang, X. Wang, *J. Mater. Chem. A* **2019**, *7*, 5069.

[7] S. Li, X. Wang, X. Chi, Y. Xiong, Y. Sun, Z. Tang, X. Gao, H. Zhang, J. Li, K. Nie, J. Xie, Z. Y. Yang, Y. M. Yan, *Adv. Funct. Mater.* **2023**, *33*, 2306098.

[8] X. Lin, Y. C. Huang, Z. Hu, L. Li, J. Zhou, Q. Zhao, H. Huang, J. Sun, C. W. Pao, Y. C. Chang, H. J. Lin, C. Te Chen, C. L. Dong, J. Q. Wang, L. Zhang, *J. Am. Chem. Soc.* **2022**, *144*, 416.

[9] X. Wang, Y. Tang, J. M. Lee, G. Fu, *Chem Catal.* **2022**, *2*, 967.

[10] X. Ren, F. Hou, F. Wang, X. Zhang, Q. Wang, *Int. J. Hydrogen Energy* **2018**, *43*, 22529.

[11] H. S. Jadhav, H. A. Bandal, S. Ramakrishna, H. Kim, *Adv. Mater.* **2022**, *34*, 2107072.

[12] B. Singh, P. Mannu, Y. C. Huang, R. Prakash, S. Shen, C. L. Dong, A. Indra, *Angew. Chem., Int. Ed.* **2022**, *61*, 2211585.

[13] B. Singh, O. Prakash, P. Maiti, A. Indra, *ACS Appl. Nano Mater.* **2020**, *3*, 6693.

[14] P. Roy Chowdhury, H. Medhi, K. G. Bhattacharyya, C. Mustansar Hussain, *Coord. Chem. Rev.* **2023**, *483*, 215083.

[15] Q. Dong, C. Shuai, Z. Mo, N. Liu, G. Liu, J. Wang, H. Pei, Q. Jia, W. Liu, X. Guo, *J. Solid State Chem.* **2021**, *296*, 121967.

[16] P. Maurya, V. Vyas, A. N. Singh, A. Indra, *Chem. Commun.* **2023**, 7200.

[17] R. Yang, Y. Zhou, Y. Xing, D. Li, D. Jiang, M. Chen, W. Shi, S. Yuan, *Appl. Catal. B Environ.* **2019**, *253*, 131.

[18] Q. sheng Zhou, X. wen Peng, L. xin Zhong, R. cang Sun, *Environ. Sci. Ecotechnology* **2020**, *1*, 100004.

[19] H. Xu, B. Wang, C. Shan, P. Xi, W. Liu, Y. Tang, *ACS Appl. Mater. Interfaces* **2018**, *10*, 6336.

[20] Y. Li, X. Zhang, Z. Zheng, *Small* **2022**, *18*, 2107594.

[21] S. Li, E. Li, X. An, X. Hao, Z. Jiang, G. Guan, *Nanoscale* **2021**, *13*, 12788.

[22] B. Singh, A. Indra, *Dalt. Trans.* **2021**, *50*, 2359.

[23] Y. Hu, Z. Wang, W. Liu, L. Xu, M. Guan, Y. Huang, Y. Zhao, J. Bao, H. M. Li, *ACS Sustain. Chem. Eng.* **2019**, *7*, 16828.

[24] T. Bhowmik, M. K. Kundu, S. Barman, *ACS Appl. Energy Mater.* **2018**, *1*, 1200.

[25] K. Bera, A. Karmakar, S. Kumaravel, S. Sam Sankar, R. Madhu, H. N Dhandapani, S. Nagappan, S. Kundu, *Inorg. Chem.* **2022**, *61*, 4502.

[26] L. Wen, X. Zhang, J. Liu, X. Li, C. Xing, X. Lyu, W. Cai, W. Wang, Y. Li, *Small* **2019**, *15*, 1902373.

[27] X. Yang, J. Cheng, Y. Xu, H. Li, W. Tu, J. Zhou, *Chem. Eng. J.* **2023**, *472*, 145076.

[28] S. Zhu, J. Wang, H. Li, J. Cai, Y. Li, J. Hu, Y. He, Y. Zhou, *ACS Appl. Nano Mater.* **2022**, *5*, 13047.

[29] Y. Lin, H. Wang, C. K. Peng, L. Bu, C. L. Chiang, K. Tian, Y. Zhao, J. Zhao, Y. G. Lin, J.

M. Lee, L. Gao, *Small* **2020**, *16*, 2002426.

[30] J. X. Feng, S. H. Ye, H. Xu, Y. X. Tong, G. R. Li, *Adv. Mater.* **2016**, *28*, 4698.

[31] M. C. Sung, G. H. Lee, D. W. Kim, *J. Alloys Compd.* **2019**, *800*, 450.

[32] D. Zhao, Y. Pi, Q. Shao, Y. Feng, Y. Zhang, X. Huang, *ACS Nano* **2018**, *12*, 6245.

[33] Y. Liu, C. Ma, Q. Zhang, W. Wang, P. Pan, L. Gu, D. Xu, J. Bao, Z. Dai, *Adv. Mater.* **2019**, *31*, 1900062.

[34] M. Dinari, H. Allami, M. M. Momeni, *Energy and Fuels* **2021**, *35*, 1831.

[35] M. Rong, H. Zhong, S. Wang, X. Ma, Z. Cao, *Colloids Surfaces A Physicochem. Eng. Asp.* **2021**, *625*, 126896.

[36] S. Xu, C. Lv, T. He, Z. Huang, C. Zhang, *J. Mater. Chem. A* **2019**, *7*, 7526.

[37] Y. R. Zheng, M. R. Gao, Q. Gao, H. H. Li, J. Xu, Z. Y. Wu, S. H. Yu, *Small* **2015**, *11*, 182.

[38] X. Du, Y. Ding, X. Zhang, *Appl. Surf. Sci.* **2021**, *562*, 150227.

[39] H. Xu, J. Cao, C. Shan, B. Wang, P. Xi, W. Liu, Y. Tang, *Angew. Chem., Int. Ed.* **2018**, *57*, 8654.

[40] X. Wu, T. Zhang, J. Wei, P. Feng, X. Yan, Y. Tang, *Nano Res.* **2020**, *13*, 2130.

[41] X. Yang, Z. Tao, Y. Wu, W. Lin, J. Zheng, *J. Alloys Compd.* **2020**, *828*, 154394.

[42] F. Dionigi, J. Zhu, Z. Zeng, T. Merzdorf, H. Sarodnik, M. Gliech, L. Pan, W. X. Li, J. Greeley, P. Strasser, *Angew. Chem., Int. Ed.* **2021**, *60*, 14446.

[43] S. Anantharaj, S. Kundu, *ACS Energy Lett.* **2019**, *4*, 1260.

[44] S. Anantharaj, S. Kundu, *ACS Energy Lett.* **2019**, *4*, 1260.

[45] P. Liu, B. Chen, C. Liang, W. Yao, Y. Cui, S. Hu, P. Zou, H. Zhang, H. J. Fan, C. Yang, *Adv. Mater.* **2021**, *33*, 2007377.

[46] K. Dastafkan, X. Shen, R. K. Hocking, Q. Meyer, C. Zhao, *Nat. Commun.* **2023**, *14*, 36100.

[47] G. Qian, J. Chen, T. Yu, J. Liu, L. Luo, S. Yin, *Nano-Micro Lett.* **2022**, *14*, 744.

[48] S. S. Jeon, P. W. Kang, M. Klingenhof, H. Lee, F. Dionigi, P. Strasser, *ACS Catal.* **2023**, *13*, 1186.

[49] X. Zhenga, J. Tanga, A. Galloc, J. A. G, Torresc, X. Yua, C. J. Athanitisa, E. M, Beena, P. Erciusd, H. Maoe, S. C. Fakraf, C. Songd, R. C. Davisg, J. A. Reimere, J. Vinsonh, M. Bajdichc, Y. Cuia, *PNAS*. **2021**, *118*, e2101817118.

[50] G. Murugadoss, D. D. Kumar, M. R. Kumar, N. Venkatesh, P. Sakthivel, *Sci. Rep.* **2021**, *11*, 79993.

[51] W. Wang, Y. Hu, S. Chen, *Chem. Commun.* **2022**, *58*, 11406.